ADVANCED FUNCTIONAL MATERIALS
www.afm-journal.de

An All-Ceramic Solid-State Rechargeable Na^+-Battery Operated at Intermediate Temperatures

*Tao Wei, Yunhui Gong, Xuan Zhao, and Kevin Huang**

A major challenge to the development of the next-generation all-solid-state rechargeable battery technology is the inferior performance caused by insufficient ionic conductivity in the electrolyte and poor mixed ionic-electronic conductivity in the electrodes. Here we demonstrate the utility of elevated temperature as an advantageous means of enhancing the conductivity in the electrolyte and promoting the catalytic activity at electrodes in an all-ceramic rechargeable Na^+-battery. The new Na^+-battery consists of a 154-μm thick Na-β''-Al_2O_3 electrolyte membrane, a 22-μm thick P_2-$Na_{2/3}[Fe_{1/2}Mn_{1/2}]O_2$ cathode and 52-μm thick $Na_2Ti_3O_7$-$La_{0.8}Sr_{0.2}MnO_3$ composite anode. The battery is shown to be capable of producing a reversible and stable capacity of 152 $mAhg^{-1}$ at 350 °C. While the battery's achievable capacity is limited by the electrode materials employed, it does exhibit unique low self-discharge rate, high tolerance to thermal cycling and an outstanding safety feature.

1. Introduction

Development of high-capacity, operationally safe, mechanically robust, and cost-effective rechargeable battery systems is one of the most desirable technological advancements to enable a widespread deployment of all-electric vehicles, renewable energy and smart grid infrastructure of our future. The modern rechargeable batteries use two primary types of electrolyte solutions, viz. aqueous and organic solvents, to support the migration of the working ion. Batteries based on aqueous electrolytes have low voltage and energy capacity, but safe to operate. In contrast, those based on organic electrolytes exhibit 2–3 times higher voltage and energy density than the former, but unsafe to operate, particularly at high charging/discharging rates. The cause for the un-safety of high-voltage and high-rate rechargeable batteries is deeply rooted in the accelerated chemical reactions between the organic solvent and solid electrodes, releasing a significant amount of heat and causing "thermal runaway". One of the viable solutions to this problem is to adopt a solid electrolyte with which solid electrodes would not react, even at high cycling rates.

Another issue associated with the current organic-electrolyte-based high-voltage and high-capacity rechargeable batteries, e.g. lithium-ion batteries (LIBs), is the cost of lithium. Lithium is a light element neither earth-abundant (ranked the 25th of the most abundant elements) nor evenly distributed geologically on the earth. It is, therefore, a relatively expensive element, roughly 30 times more expensive than sodium, another light alkaline element.[1,2]

Based on these facts, it would seem to be rational to develop all-solid-state sodium-ion batteries (NIBs) that are advantageous in both cost and safety, even though they may exhibit slightly lower Nernst potential than LIBs due to thermodynamic reasons. In fact, NIBs have been investigated for nearly half a century. The most successful demonstration is the sodium-sulfur (NAS) and ZEBRA rechargeable batteries operated at 250–350 °C, in which a ceramic Na^+-conductor, Na-β''-Al_2O_3, is used as the electrolyte to separate two molten Na/Na_xS and $Na/NiCl_2$ anode/cathode pairs for NAS and ZEBRA, respectively.[1,3–5] However, active molten Na is a chemical hazard to safe operations. Extra safety measures have to be taken into account, which in turn increases the overall system cost. Furthermore, the molten state of Na needs to be maintained all the time, even when the battery is not in operation, in order to avoid a disastrous "freezing" effect. This requirement costs an additional >10% of its own capacity per day.[6] The NAS/ZEBRA battery technology, therefore, will need to overcome the "molten electrodes" barriers in order to become a safe and commercially viable product.[3] On the other hand, NIBs have also been demonstrated with good room-temperature performance in recent years with liquid electrolytes and solid-state electrodes.[7–10]

The all-solid-state rechargeable batteries have been considered the next-generation energy storage devices because of their unequivocal advantages over liquid-based counterparts in thermal and chemical stabilities, mechanical robustness, cost and safety.[11–13] The all-solid-state Li^+ and Na^+ rechargeable batteries are the most studied systems due to the availability of solid Li^+/Na^+ conductors and a long history of research. So far, all-solid-state LIBs have been demonstrated with solid Li^+-conductors such as garnet $Li_5La_3M_2O_{12}$ (M = Nb, Ta),[14,15] perovskite $La_{0.5}Li_{0.5}TiO_3$[16] and thio-LISICON $Li_{3.25}Ge_{0.25}P_{0.75}S_4$[17,18] as the electrolyte, $LiCoO_2$ as the cathode and Li/C as the anode.[15,18,19] A multilayered ceramic-based LIB comprising of a $Li_{1.5}Al_{0.5}Ge_{1.5}(PO_4)_3$ as the electrolyte and $Li_3V_2(PO_4)_3$ as both cathode and anode has recently been fabricated by spark plasma sintering.[20,21] Similarly, all-solid-state NIBs have also been reported with NASICON ($Na_3Zr_2Si_2PO_{12}$) as the electrolyte,

T. Wei, Y. Gong, X. Zhao, K. Huang
Department of Mechanical Engineering
University of South Carolina
Columbia SC29201
Tel: 803–777–0204
E-mail: huang46@cec.sc.edu

DOI: 10.1002/adfm.201400773

$Na_3V_2(PO_4)_3$ as both the cathode and anode.[22,23] However, the main issue identified from these early developments is the inferiority in capacity, working voltage and cyclic stability. A fundamental reason for the low performance is the insufficient ionic conductivity in solid electrolytes and poor mixed ionic and electronic conductivity in electrodes at ambient temperature under which these batteries were usually tested.

While discovering new high-conductivity materials for all-solid-state batteries is on the horizon, elevating the operating temperature to a manageable level such as 250–350 °C represents a simple and viable solution to increasing ionic conductivity in the electrolyte and boosting catalytic activity at the electrodes. This vision is shared by General Electric who is currently developing an intermediate-temperature sodium chloride battery system (Durathon Battery) similar to ZEBRA for hybrid locomotives.[24] Elevated operating temperature is no longer deemed as a critical issue since the engineering experience gained from the early NAS/ZEBRA development enabling the design of robust and reliable thermal systems can be readily applied to the newer intermediate-temperature battery systems. Therefore, the aforementioned advantages of ceramic-based intermediate-temperature batteries can be fully exploited for enhanced performance.

The objective of this study is to exploit the full potential of an intermediate-temperature all-ceramic Na^+-battery comprising of a Na-β''-Al_2O_3 electrolyte, P_2-$Na_{2/3}[Fe_{1/2}Mn_{1/2}]O_2$ cathode, and $Na_2Ti_3O_7$-$La_{0.8}Sr_{0.2}MnO_3$ composite anode, by systematically testing its electrochemical performance under different conditions of C-rates, temperatures, thermal transients and self-discharge. While the properties of the battery materials employed in this study have been previously studied by other groups, to the best of our knowledge, assembling and testing them in a full battery fashion within the intermediate-temperature range (250–350 °C) represents a new work.

2. Results and Discussion

2.1. Property of the Battery Materials

The phases in the synthesized Na-β''-Al_2O_3 identified by XRD (see Figure S1 in the Supporting Information) consist of a primary Na-β''-Al_2O_3 crystallized in rhombohedral structure (space group *R-3m*) with a minor $Li_{1.9}Na_2Al_{12}O_{19.95}$ impurity, which is very common in the synthesis of Na-β''-Al_2O_3. In contrast, XRD revealed (see Figure S2,S3 in the SI) that the cathode NFMO crystallized in a hexagonal structure (space group *P63/mmc*) and anode NTO crystallized in a monoclinic structure (space group *P21/m*). These crystal structures are consistent with those reported in the literature.

The bulk conductivities of dense Na-β''-Al_2O_3, NFMO and NTO pellets measured in air are shown in **Figure 1** as an Arrhenius plot. As a fast ionic conductor, Na-β''-Al_2O_3 exhibited high conductivity, e.g., 0.1 S cm^{-1} at 300 °C, which is consistent with the literature.[4,25,28] The NFMO cathode also showed a reasonably high conductivity of ≈0.1 S cm^{-1} at 350 °C benefiting from the mixed valence state held by Fe and Mn. However, the conductivity of the anode NTO is much lower than the above two materials. The comparison in Figure 1 indicates 2–3 orders of magnitude lower conductivity in NTO than Na-β''-Al_2O_3 and NFMO. To enhance the electronic conductivity of the NTO anode, 40 vol% of a low-cost electronic conductor $La_{0.8}Sr_{0.2}MnO_{3-\delta}$ (LSM) was blended into the NTO to form a composite anode, although other electronic conductors such as Pt, silver and carbon could also be considered. Since the intrinsic conductivity present in the NTO is primarily ionic (Na^+) in nature, the addition of an electronic component would make the resultant composite a much preferred mixed ionic and electronic conductor. The comparison of XRD patterns among NTO, LSM and NTO+LSM (see Figure S4 in the SI) indicates no reaction occurred between NTO and LSM even after sintering at 950 °C. Evident from Figure 1, the total conductivity of the composite NTO+LSM anode has been significantly increased to the level of Na-β''-Al_2O_3 and NFMO by the presence of LSM.

The average thermal expansion coefficients (TECs) of the Na-β''-Al_2O_3 electrolyte, NFMO cathode, NTO and NTO+LSM anode are shown in **Figure 2**. From RT to 400 °C, it is evident that the average TEC of the electrolyte matches well with that of the NTO anode, 6.2×10^{-6} K^{-1} vs 5.1×10^{-6} K^{-1}. The TECs of NFMO cathode and NTO+LSM anode match well, 11.6×10^{-6} K^{-1} and 10.2×10^{-6} K^{-1}, but are higher than that of the electrolyte. With 40 vol% addition of LSM into NTO, the TEC of the

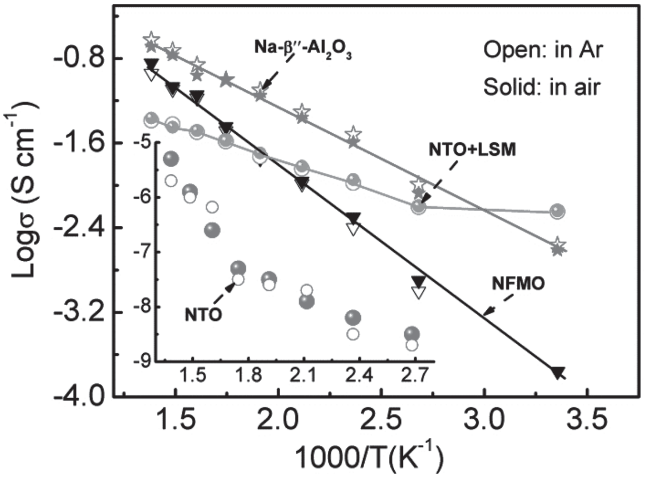

Figure 1. Electrical conductivity of Na-β''-Al_2O_3, NFMO, NTO and NTO+LSM.

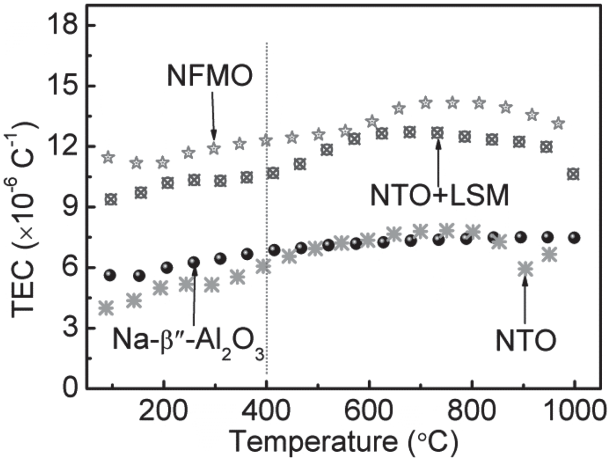

Figure 2. Thermal expansion coefficients of Na-β''-Al_2O_3, NFMO, NTO and NTO+LSM anode measured from room temperature to 1000 °C in air.

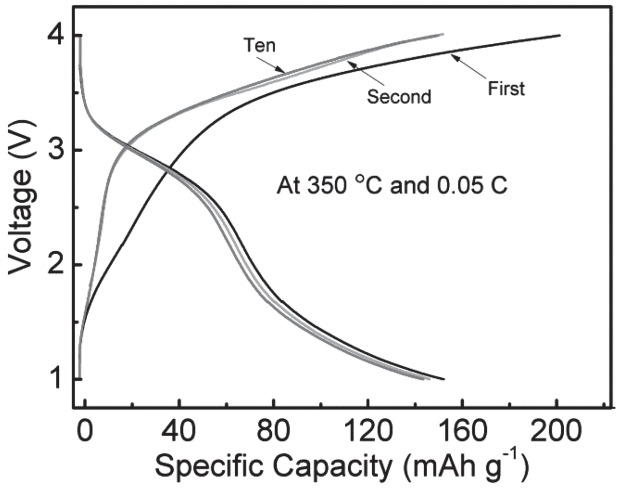

Figure 3. The first, second and tenth charge/discharge profiles for the solid-state Na^+-battery: NFMO/Na-β''-Al_2O_3/NTO+LSM; electrolyte thickness: 154 μm.

resultant composite has been elevated to the level close to that of LSM, $\approx 11.0 \times 10^{-6}$ K^{-1}.

2.2. Electrochemical Performance

The first, second and tenth charge/discharge cycle curves of the full battery: NFMO/Na-β''-Al_2O_3/NTO+LSM, cycled within a voltage window of 1–4 volt, at a rate of 0.05 C at 350 °C are shown in **Figure 3**. During the first cycle, the specific charging capacity reached 203 $mAhg^{-1}$, while the discharge capacity was merely 152 $mAhg^{-1}$, indicating 51 $mAhg^{-1}$ or ≈26% irreversible capacity loss during the first cycle. As indicated in the literature,[26,29] this initial capacity loss is possibly associated with the irreversible extraction of Na^+ originally occupying stacking faults in the NFMO, which becomes inaccessible to Na^+-insertion during the discharge.

After the first cycle, there was very little capacity loss observed, and the shuttling of Na^+ between the energetically favorable Na-sites in the cathode and in the anode becomes reversible. This reversible Na^+-shuttling is essential for a functional operation of the all-ceramic rechargeable Na^+-battery investigated.

The temperature effect on the charge/discharge behavior of the battery is shown in **Figure 4**a. The specific capacities for the charge and discharge reached 155 and 152 $mAhg^{-1}$ at 350 °C, respectively; 152 $mAhg^{-1}$ represents an equivalent of 58% of the NFMO-cathode's theoretical capacity calculated from a single-electron process of Me^{3+}/Me^{4+} ($Me = Fe_{1/2}Mn_{1/2}$) redox couple. From the cycling profiles, the electrochemical redox reactions, particularly at higher temperatures, occur in two steps. This observation is consistent with results obtained from previous half-cell studies where two plateaus were observed for the NFMO cathode[20] and one for the NTO anode.[21] However, the positions of the two plateaus observed in this study are different from those reported, viz., the two plateaus on the discharge curve lie mainly below and above 2.5 V, whereas the two discharge plateaus observed in half-cell and at RT lie mainly below and above 3.2 V. The lowered plateau levels are probably caused by the use of NTO anode since the latter is known for its 0.4 V charging plateau. Another factor for the lowered plateaus could also be related to the elevated temperature.

As the temperature decreases, Figure 4a indicates that the specific discharge capacity decreases, viz. 152 mAh g^{-1}@350 °C→121 mAh g^{-1}@300 °C→67 mAh g^{-1}@250 °C. While increased polarization by lowered temperature is responsible for the capacity loss, it is interesting to note that there is an appreciable loss of specific capacity at temperatures below 300 °C. Although the present study was not focused on understanding the behavior, a further optimization of materials properties and multilayered structure can be leveraged for reducing capacity's sensitivity to temperature.

The effect of C-rate on the capacity at 350 °C is shown in Figure 4b. The reversible discharge specific capacity is evidently decreased from 152 to 31 mAh g^{-1} by increasing C-rate from 0.05 C to 5 C. This decrease is obviously caused by the increased polarization losses (IR) at higher C-rate, a phenomenon universally true for any type of batteries with internal resistance. Unfavorable Na^+-transport kinetics and un-optimized interfacial structures are responsible for the polarization loss.

The battery's ability to retain the capacity over repeated cycles is shown in **Figure 5** for 0.05 C and 1 C. Under these two rates, except the 1st cycle, >98% cycle efficiency was achieved

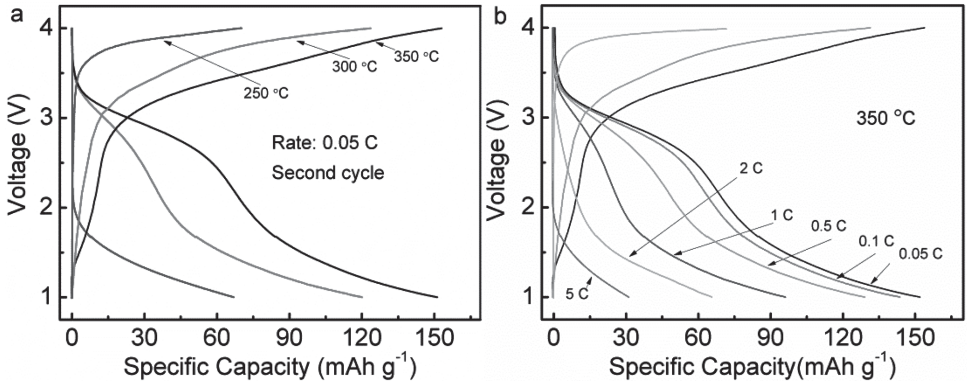

Figure 4. The 2nd -cycle charge and discharge profiles. a) Temperature effect at 0.05 C; b) C-rate effect at 350 °C. The voltage window cycled: 1–4 V; electrolyte thickness: 154 μm.

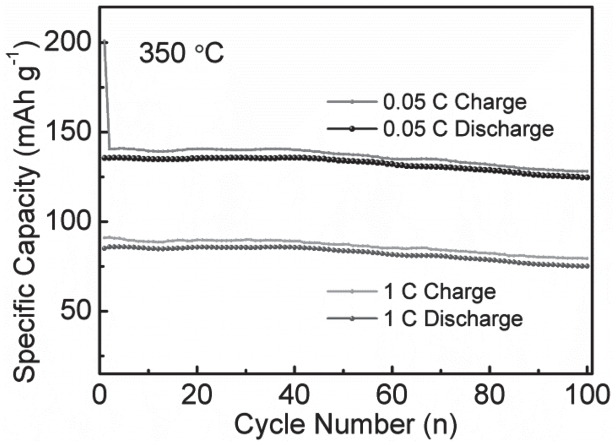

Figure 5. Plot of specific capacity vs number of cycle. Voltage window cycled: 1–4 V; electrolyte thickness: 195 μm.

with >90% capacity retention after 100 cycles. The capacity stability is clearly benefited from the ceramic materials used in the battery, which is free of electrolyte decomposition and electrolyte-electrode interactions. A slightly lower specific capacity in Figure 5 than in Figure 4 is stemmed from a thicker electrolyte membrane employed (154 μm vs 195 μm).

As aforementioned, an NAS battery would consume >10% of its own capacity per day to maintain its operating temperature even when not in use in order to avoid a disastrous "freezing" effect. For the solid-state ceramic NIB such as the one investigated in this study, however, maintaining a "hot" condition is no longer a requirement. When not in use, the all ceramic NIB with loaded capacity can be allowed to cool down to ambient temperature (RT). This advantage is clearly demonstrated in **Figure 6**, where capacity of the battery at 350 °C was first loaded by charging it to 4 V at 0.1 C, followed by cooling it down to RT. After 100 h, the battery was brought back to 350 °C in 10 minutes and cycled at 0.1 C before cooling down to RT again. After another 1 month, the battery was brought back to 350 °C in 10 minutes and cycled under the same condition. It

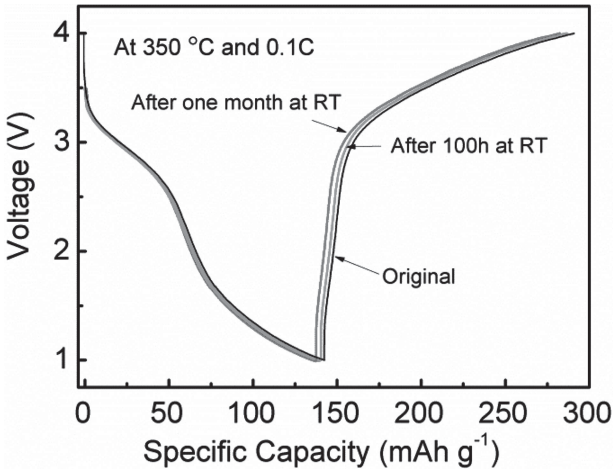

Figure 6. Capacity retention after battery being thermally cycled and staged at RT.

is evident from Figure 6 that there is little difference in performance resulting from either the fast thermal cycling or the time-at-RT when compared with the original performance (black curve), demonstrating the robustness of the all ceramic NIB to thermal stresses and nearly zero self-discharge rate.

One critical factor impacting the thermal transient characteristic of the all-ceramic battery is the mismatch in thermal expansion coefficients (TECs) among all adjacent components. Figure 2 shows that the TECs of the anode (NTO+LSM) and the cathode NFMO match well from RT to 400 °C, but not with the electrolyte. While the present study did not reveal the adverse effect by the TEC mismatch, we do acknowledge that a closer match in TECs among functional layers, in particular with anisotropic expansion in the layered 2D NFMO cathode, should be considered for future material research and engineering design.

3. Conclusions

The present study demonstrates the fabrication and performance of an all-solid-state Na^+-battery made of ceramic-oxide-based functional layers and operated at intermediate temperatures. Elevating the operating temperature to a manageable level such as 250–350 °C has been utilized as an advantageous means of promoting the performance. Compared with the early solid-state LIBs and NIBs, the performance of the new all-ceramic NIB is superior in voltage, capacity, reversibility and stability. In addition, the battery exhibited excellent tolerance to thermal cycling, very low self-discharge rate and a sound safety feature. These unique attributes promise the new all-ceramic Na^+-battery to be a valuable asset for stationary and transportation energy storage applications.

4. Experimental Section

Synthesis of Battery Materials: The Na-β''-Al_2O_3 electrolyte was prepared by a two-step $NaAl_5O_8$-$LiAl_5O_8$ reaction synthesis procedure as described in Li et al.[25] Precursor $NaAl_5O_8$ was first synthesized from a sol-gel method. Stoichiometric amounts of $Al(NO_3)_3{\cdot}9H_2O$ and $NaNO_3$ in 60% excess over stoichiometry were first dissolved into DI water with citric acid as the complexing agent. A gel was formed after stirring and heating on a hot plate, then decomposed at 400 °C for 10 h to form a carbonaceous powder. After grinding, the powder was fired at 800 °C to fully convert it into oxide. The $NaAl_5O_8$ precursor was finally obtained by calcining at 1250 °C for 2 h. The $LiAl_5O_8$ precursor was synthesized by a similar method but with 10% excess $LiNO_3$ reacting with $Al(NO_3)_3{\cdot}9H_2O$. The separately synthesized $NaAl_5O_8$ and $LiAl_5O_8$ precursors were then mixed together in a stoichiometric ratio to yield $Na_{1.67}Al_{10.67}Li_{0.33}O_{17}$ (a type of Na-β''-Al_2O_3) by high-energy ball milling, pressing into pellets, and finally sintering at 1600 °C for 1 hour to obtain a dense membrane.

The layer-structured P_2-$Na_{2/3}[Fe_{1/2}Mn_{1/2}]O_2$ (NFMO) cathode material was synthesized according to ref. [26]. Stoichiometric amounts of Na_2CO_2 (99.6% Acros Organics), Fe_2O_3 (99.9%, Alfa Aesar) and Mn_2O_3 (99%, Strem Chemical, Inc) with a molar ratio of 2/3:1/2:1/2 were carefully weighed, intimately mixed, intensely ball-milled, and then pressed into pellets. The pellets were fired at 900 °C for 12 h. The $Na_2Ti_3O_7$ (NTO) anode was synthesized also via a solid-state reaction according to ref. [27]. Anatase TiO_2 and about 5% excess of NaOH over stoichiometry were intimately mixed, intensely ball-milled and pelletized. The pellets were then calcined in air at 800 °C for 20 h. In order to increase the electronic conductivity of the NTO anode, 40 vol% of an electronic conductor $La_{0.8}Sr_{0.2}MnO_{3+\delta}$ (LSM, purchased from Fuel

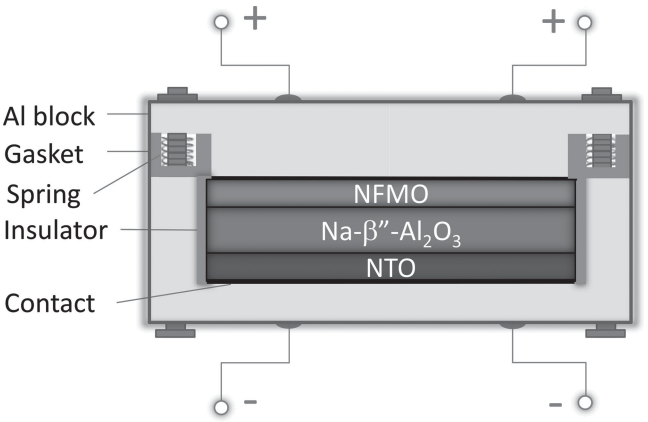

Figure 7. Schematic of the setup for testing the ceramic-based rechargeable Na^+-battery

Cell Materials, Ohio, USA) was also blended into the NTO to form a composite anode for the battery.

Assembly of Battery: A Na-β''-Al_2O_3 electrolyte-supported battery structure was adopted for the performance evaluation. The thicknesses of the Na-β''-Al_2O_3 electrolytes fabricated varied in three levels: 154, 166 and 195 μm, for different characterization purposes. The NFMO cathode and LSM-incorporated NTO powders pulverized from the sintered pellets were first made into ethanol-based suspensions, followed by air spraying them on the two sides of the electrolyte membrane and drying at 80 °C for 30 minutes. The three-layer structure was finally fired at 950 °C for 1 h to achieve good bonding strength. Pt paste/meshes were attached on the surfaces of the electrodes as the contact layer. The multilayer structure was then sealed in a spring-loaded Al-block enclosure shown in **Figure 7**. The top and bottom Al blocks were also used as the current collector.

Electrochemical Testing: A Solartron 1260/1287 Electrochemical System was employed to characterize the electrical performance of the battery with software modules such as galvanic cycles. The battery was cycled from 1 to 4 volts under different C-rates (or current densities), from which the specific capacity was calculated based on the mass of the NFMO cathode. The operating temperature was varied from 250 to 350 °C. To study the self-discharge rate and thermal cycleability, the NIBs investigated were also subject to the events of rapid cooling from 350 °C to RT by shutting off furnace, staging at RT for 100 hours and one month, respectively, and then rapidly heating back to 350 °C within 10 minutes to examine its ability to retain capacity.

Other Characterization: The phase purity of all the three functional materials synthesized was examined by powder X-ray diffraction (PXRD) with an X-ray diffractometer (D/max-A, Rigaku, Japan) with graphite-monochromatized Cu-Kα radiation (λ = 1.5418 Å). The XRD scan was performed at a rate of 5° min^{-1} from 2θ = 20 to 80 °. The XRD patterns were further analyzed with the JADE (MDI) software to identify phase structure and compositions.

The bulk conductivities of dense Na-β''-Al_2O_3, NFMO, NTO and LSM-incorporated NTO (NTO+LSM) pellets were measured from RT to 450 °C in air and Ar, respectively, with electrochemical impedance spectroscopy. The pellets were roughly 3–5 mm in thickness and 13 mm in diameter.

The microstructural features of the fabricated battery were captured and analyzed with a field emission scanning electron microscope (FESEM, Zeiss Ultra) equipped with an energy dispersive X-ray spectroscopy (EDS) analyzer.

The thermal expansions of the three functional materials were measured in air with a Theta 1600 dilatometer in the temperature range of RT-1000 °C. The samples were sintered rectangular bars 4 × 4 mm in cross-section and 25 mm in length. The coefficient of thermal expansion was determined as the derivative of linear expansion with regard to temperature from the expansion curves recorded.

Supporting Information

Supporting Information is available from the Wiley Online Library or from the author.

Received: March 9, 2014
Revised: April 16, 2014
Published online: June 24, 2014

[1] M. D. Slater, D. Kim, E. Lee, C. S. Johnson, *Adv. Funct. Mater.* **2013**, *23*, 947.
[2] Z. Yang, J. Zhang, M. C. W. Kintner-Meyer, X. Lu, D. Choi, J. P. Lemmon, J. Liu, *Chem. Rev.* **2011**, *111*, 3577.
[3] Z. Wen, Y. Hu, X. Wu, J. Han, Z. Gu, *Adv. Funct. Mater.* **2013**, *23*, 1005.
[4] N. Baffier, J. C. Badot, P. Colomban, *Mater. Res. Bull.* **1981**, *16*, 259.
[5] P. W. Haycock, W. Hayes, R. C. C. Ward, C. J. Salter, R. J. Harverson, *Solid State Ionics* **1995**, *80*, 53.
[6] K. B. Hueso, M. Armand, T. Rojo, *Energy Environ. Sci.* **2013**, *6*, 734.
[7] H. Pan, Y. Hu, L. Chen, *Ener. Environ. Sci.* **2013**, *6* , 2338.
[8] H. Pan, X. Lu, X. Yu, Y. Hu, H. Li, X. Yang, L. Chen, *Adv. Energy Mater.* **2013**, *3*, 1186.
[9] Y. Wang, X. Yu, S. Xu, J. Bai, R. Xiao, Y. Hu, H. Li, X. Yang, L. Chen, X. Huang, *Nat. Comm.* **2013**, *4*, 2365.
[10] Z. Jian, C. Yuan, W. Han, X. Lu, L. Gu, X. Xi, Y. Hu, H. Li, W. Chen, D. Chen, Y. Ikuhara, L. Chen, *Adv. Funct. Mater.* DOI: 10.1002/adfm.201400173.
[11] K. Brandt, *Solid State Ionics* **1994**, *69*, 173.
[12] M. S. Whittingham, *Chem. Rev.* **2004**, *104*, 4271.
[13] C. A. Vincent, *Solid State Ionics* **2000**, *134*, 159.
[14] Y. Jin, P. J. McGinn, *J. Power Sources* **2013**, *239*, 326.
[15] S. Ohta, S. Komagata, J. Seki, T. Saeki, S. Morishita, T. Asaoka, *J. Power Sources* **2013**, *238*, 53.
[16] Y. Inaguma, C. Liquan, M. Itoh, T. Nakamura, T. Uchida, H. Ikuta, M. Wakihara, *Solid State Comm.* **1993**, *86*, 689.
[17] R. Kanno, M. Murayama, *J. Electrochem. Soc.* **2001**, *148*, A742.
[18] N. Kamaya, K. Homma, Y. Yamakawa, M. Hirayama, R. Kanno, M. Yonemura, T. Kamiyama, Y. Kato, S. Hama, K. Kawamoto, A. Mitsui, *Nat. Mater.* **2011**, *10*, 682.
[19] P. Novák, Y. Geronov, B. Puresheva, P. Podhájecky, B. Klápště, P. Zlatilova, *J. Power Sources* **1989**, *28*, 279.
[20] G. Delaizir, V. Viallet, A. Aboulaich, R. Bouchet, L. Tortet, V. Seznec, M. Morcrette, J.-M. Tarascon, P. Rozier, M. Dollé, *Adv. Funct. Mater.* **2012**, *22*, 2140.
[21] A. Aboulaich, R. Bouchet, G. Delaizir, V. Seznec, L. Tortet, M. Morcrette, P. Rozier, J.-M. Tarascon, V. Viallet, M. Dollé, *Adv. Energy Mater.* **2011**, *1*, 179.
[22] F. Lalère, J. B. Leriche, M. Courty, S. Boulineau, V. Viallet, C. Masquelier, V. Seznec, *J. Power Sources* **2014**, *247*, 975.
[23] Y. Noguchi, E. Kobayashi, L. S. Plashnitsa, S. Okada, J.-i. Yamaki, *Electrochimica Acta* **2013**, *101*, 59.
[24] http://www.ecomagination.com/portfolio/durathon-battery (June 6, 2014)
[25] N. Li, Z. Wen, Y. Liu, X. Xu, J. Lin, Z. Gu, *J. Eur. Ceram. Soc.* **2009**, *29*, 3031.
[26] N. Yabuuchi, M. Kajiyama, J. Iwatate, H. Nishikawa, S. Hitomi, R. Okuyama, R. Usui, Y. Yamada, S. Komaba, *Nat. Mater.* **2012**, *11*, 512.
[27] A. Rudola, K. Saravanan, C. W. Mason, P. Balaya, *J. Mater. Chem. A* **2013**, *1*, 2653.
[28] H. Näfe, S. Cheng-wen, *Solid State Ionics* **1996**, *86–88*, 773.
[29] G. Singh, B. Acebedo, M. Cabanas, D. Shanmukaraj, M. Armand, T. Rojo, *Electrochem. Comm.* **2013**, *37*, 61.